INL/JOU-20-60203-Revision-0

Modeling brittle fracture due to anisotropic thermal expansion in polycrystalline materials

June 2021

Aashique Rezwan, Michael Tonks, Andrea M Jokisaari

Changing the World's Energy Future

Idaho National Laboratory

INL is a U.S. Department of Energy National Laboratory operated by Battelle Energy Alliance, LLC

INL/JOU-20-60203-Revision-0

Modeling brittle fracture due to anisotropic thermal expansion in polycrystalline materials

Aashique Rezwan, Michael Tonks, Andrea M Jokisaari

June 2021

Idaho National Laboratory
Idaho Falls, Idaho 83415

http://www.inl.gov

Prepared for the
U.S. Department of Energy
Under DOE Idaho Operations Office
Contract DE-AC07-05ID14517, DE-AC07-05ID14517

Highlights

Modeling Brittle Fracture due to Anisotropic Thermal Expansion in Polycrystalline Materials

Aashique A Rezwan,Andrea M Jokisaari,Michael R Tonks

- Phase field fracture simulations were used to investigate the fracture of α-uranium polycrystals due to anisotropic thermal expansion.
- Cooling resulted in more severe fracture than heating due to the larger anisotropy at elevated temperatures.
- The total crack surface area decreased with decreasing grain misorientation, while the net shape changed increased.
- The thermal expansion in the [010] direction was the primary cause for fracture.

Modeling Brittle Fracture due to Anisotropic Thermal Expansion in Polycrystalline Materials

Aashique A Rezwan[a], Andrea M Jokisaari[b] and Michael R Tonks[c]

[a]Department of Mechanical Engineering, The Pennsylvania State University, University Park, PA 16801
[b]Computational Mechanics and Materials Department, Idaho National Laboratory, P.O. Box 1625, Idaho Falls, ID 83415
[c]Department of Material Science and Engineering, University of Florida, Gainesville, FL 32611

ARTICLE INFO

Keywords:
anisotropic thermal expansion
α-uranium
fracture
phase field

ABSTRACT

This work investigated brittle fracture of polycrystalline materials due to thermal stresses arising from anisotropic thermal expansion. We used phase-field fracture simulations with the properties of α-uranium (α-U) and assumed a linear elastic mechanical response. Three-dimensional simulations were used to predict fracture for various conditions and crystallographic textures. We found that fracture was more pronounced during cooling than during heating because the anisotropy increased with temperature. We also found that the total crack surface area increased with increasing average misorientation, while the net shape change of the material decreased with increasing misorientation. Two-dimensional simulations in which one crystallographic coefficient of thermal expansion (CTE) was set to zero indicated that the largest difference between the CTE in the three crystallographic directions dominates the fracture.

1. Introduction

Materials with less than cubic symmetry can have anisotropic thermal expansion, including both metals [1, 2] and ceramics [3, 4, 5, 6]. Anisotropic thermal expansion causes a net shape change in single crystals and can lead to the development of internal stresses in polycrystalline materials. In some materials, these stresses can be large enough to cause fracture. Fracture due to anisotropic thermal expansion has been studied in ceramics using experiments [3, 4, 5, 6], analytical models [7, 8, 9], and numerical simulations [8, 10]. These studies have shown that anisotropic thermal expansion results in stress concentrations at grain boundaries and triple junctions and that cracks typically nucleate at grain boundaries. Whether the impact of fracture increases or decreases with grain size depends on the material and on the nature of the application. In metals, there have been well-documented studies that thermal strain generates local microstresses [11, 12, 13, 14] in polycrystal samples that are sufficient to cause plastic deformation [11, 12] and, in some instances, brittle fracture [11, 13, 14]. However, detailed studies of fracture due to anisotropic CTE in polycrystalline metals is very limited. A detailed understanding of how anisotropic thermal expansion affects thermal microstresses and microcrack formation is important for the development of alloys for extreme thermal environments.

One difficulty in investigating fracture induced by anisotropic thermal expansion is that the engineering-scale performance of the material is significantly impacted by localized behaviors at the mesoscale, including the elastic and thermal expansion behavior of the crystal lattice, the crystallographic texture (the orientations of the grains), and the grain size. Modeling and simulation at the mesoscale using approaches like the phase-field method [15, 16] can provide a powerful means of investigating such mesoscale behaviors, because it is much easier to control the conditions and the microstructure of the material [17]. The phase-field method has become a popular method for modeling the fracture of brittle materials due to its ability to naturally represent crack nucleation and growth and to create crack surfaces [18, 19].

In this work, we investigated the impact of thermal expansion anisotropy on brittle fracture in three-dimensional polycrystals using the phase-field fracture method. We investigated the impact of both increasing and decreasing temperature and the impact of crystallographic texture. We also used 2D simulations to identify the primary cause of fracture. As a model material, we selected a highly anisotropic metal, α-uranium (α-U), and we included accurate temperature dependence of both the coefficients of thermal expansion (CTE) and elastic constants. In Section 2, a summary of the mechanical behavior of α-U is provided. In Section 3, the formulation and implementation of the model are presented. The simulation results are presented in Section 4.

2. Mechanical behavior of α-U

We investigated the impact of thermal expansion anisotropy on fracture using α-U as a model material. We selected α-U because this phenomenon has been much less studied in metals than in ceramics and because α-U is a highly anisotropic metal with available data on the impact of temperature on its CTE and elastic constants.

The crystal structure of α-U is orthorhombic, which is unusual for metals. The a, b, and c lattice constants at room temperature are 0.285 nm, 0.587 nm, and 0.495 nm, respectively [20, 21, 22]. Changes in temperature not only change the volume but also the shape of the α-U unit cell, i.e., the lattice constants do not maintain the same ratio with temper-

*Corresponding author
air5421@psu.edu (A.A. Rezwan); andrea.jokisaari@inl.gov (A.M. Jokisaari); michael.tonks@ufl.edu (M.R. Tonks)
ORCID(s):

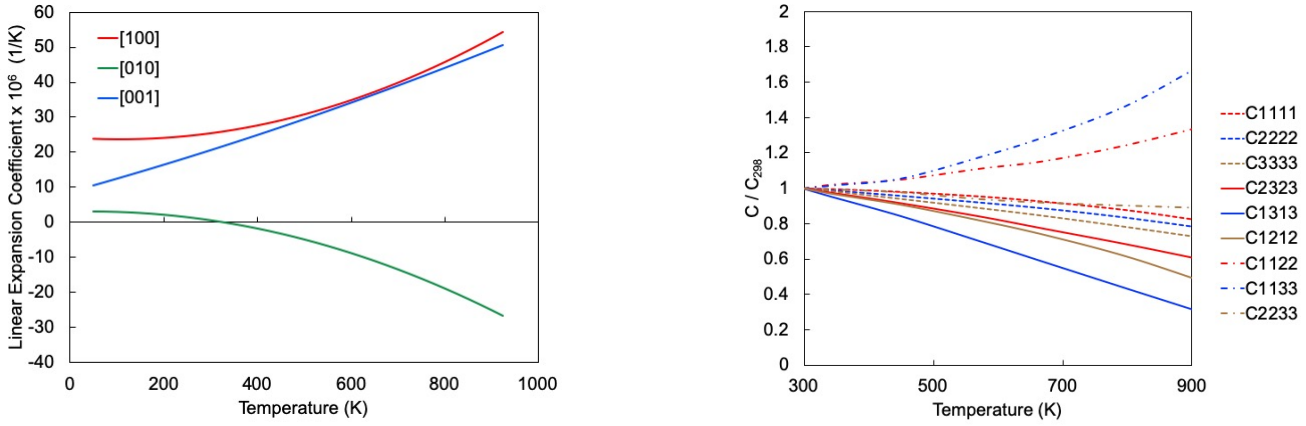

(a) (b)

Figure 1: The mechanical properties of α-U; (a) CTE versus temperature for the three crystallographic axes of α-U [1]. (b) Modulus of elasticity versus temperature, presented in the form of a normalized modulus of elasticity [26].

ature. This is defined by one CTE for each crystallographic direction: the thermal expansion exhibits a negative coefficient in the [010] direction and relatively large positive coefficients in the [100] and [001] directions [1] (Fig. 1a). Due to this anisotropy, thermal expansion of polycrystalline α-U results in significant thermal stresses between grains. In the case of thermal cycling, inter-granular void nucleation and growth have been observed over a temperature interval of greater than 200 K [23, 24]. In that work, voids mainly nucleated at carbide inclusion/matrix interfaces before intergranular fracture occurs [25]. The orthorhombic unit cell also results in highly anisotropic elastic behavior; the elasticity tensor of α-U is defined by nine unique elastic moduli. The moduli are highly temperature dependent [26], as shown in Fig. 1b. Finally, the fracture mode of α-U changes with temperature, exhibiting cleavage failure below 263 K, cleavage and intergranular fracture from 263 K to 350 K, intergranular fracture and ductile tearing from 350 K to 573 K, and only ductile tearing above 573 K [27, 28, 29]. In this work, we focus on temperatures for which intergranular brittle fracture can be assumed to be the preferred fracture mode.

3. Model Formulation and Implementation

We modeled the fracture of polycrystalline α-U induced by anisotropic thermal expansion using a phase-field fracture model. The phase-field fracture model describes fracture of brittle material using a variable field c to describe the state of the material, where $c = 0$ in intact regions, $c = 1$ in cracked regions, and $0 < c < 1$ in regions that are damaged but not fully cracked. The variable field c evolves with time to decrease the total energy of the material, including the deformation and crack surface energy. Here, we combined the phase-field fracture model with a polycrystalline description of the material including anisotropic thermal expansion and elastic constants.

Table 1
Polynomial constants for the α-U CTE fits [1].

Crystallographic Axis	$k_1^i \times 10^6$	$2k_2^i \times 10^9$	$3k_3^i \times 10^{12}$
$\alpha_{[100]}$	24.22	-9.83	46.02
$\alpha_{[010]}$	3.07	3.47	-38.45
$\alpha_{[001]}$	8.72	37.04	9.08

3.1. Anisotropic Thermal Expansion

3.1.1. Single Crystal

For a generic three-dimensional α-U single crystal, the thermal strain tensor $\boldsymbol{\epsilon}_T$ is written as

$$\boldsymbol{\epsilon}_T = \boldsymbol{\alpha}(T - T_0) \tag{1}$$

where $\boldsymbol{\alpha}$ is the second-order thermal expansion tensor, T is the absolute temperature and T_0 is the reference temperature. The thermal expansion tensor for α-U is anisotropic, meaning that its value varies depending on the crystallographic direction. The tensor is diagonal, with its diagonal values corresponding to the three CTE shown in Fig. 1a, according to

$$\boldsymbol{\alpha} = \begin{bmatrix} \alpha_{[100]} & 0 & 0 \\ 0 & \alpha_{[010]} & 0 \\ 0 & 0 & \alpha_{[001]} \end{bmatrix}. \tag{2}$$

These CTE are functions of temperature and have been fit using second order polynomials [1] according to

$$\alpha_i = k_1^i + 2k_2^i T + 3k_3^i T^2, \tag{3}$$

where $i = [100]$, $[010]$ or $[001]$ and k_1^i, k_2^i, and k_3^i are the corresponding polynomial coefficients. The values for the polynomial coefficients for temperatures ranging from 50 K to 923 K for the three CTE are given in Table 1. The stress in the material $\boldsymbol{\sigma}$ is impacted by both the elastic strain $\boldsymbol{\epsilon}$ and the thermal strains according to

$$\boldsymbol{\sigma} = \boldsymbol{C}(\boldsymbol{\epsilon} - \boldsymbol{\epsilon}_T), \tag{4}$$

where $\boldsymbol{C}$ is the single crystal elasticity tensor.

3.1.2. Polycrystal

For polycrystalline material, the model must incorporate multiple arbitrary grain rotations. An approach inspired by a phase-field model of grain growth has been implemented [30], in which a diffuse-interface description of the grains is used. Each grain g is represented by an order parameter η_g, that takes a value of $\eta_g = 1$ in the bulk of the grain, $\eta_g = 0$ outside the grain, and varies smoothly from $0 < \eta_g < 1$ across the interface between grains. These order parameters do not evolve with time but are only used to describe the static grain structure of the material. In addition, each grain has an associated orientation described by a rotation tensor $\mathbf{R}_g$. Thus, the single crystal thermal strain and elasticity tensors must be rotated to represent a given grain, such that

$$\boldsymbol{\epsilon}_T^g = \mathbf{R}_g \boldsymbol{\epsilon}_T \mathbf{R}_g^T \tag{5}$$

$$\boldsymbol{C}^g = (\mathbf{R}_g \otimes \mathbf{R}_g)\boldsymbol{C}(\mathbf{R}_g \otimes \mathbf{R}_g)^T, \tag{6}$$

where $\otimes$ is the fourth-order tensor product

$$(\mathbf{A} \otimes \mathbf{B})_{ijkl} = A_{ij} B_{kl}. \tag{7}$$

The thermal strain and elasticity tensor at a given point $\mathbf{r}$ within the material are defined by interpolating the tensors for each grain. The thermal strain $\tilde{\boldsymbol{\epsilon}}_T(T, \mathbf{r})$ is defined according to

$$\tilde{\boldsymbol{\epsilon}}_T(T, \mathbf{r}) = \frac{\sum_g \boldsymbol{\epsilon}_T^g(T) h\left(\eta_g(\mathbf{r})\right)}{\sum_g h\left(\eta_g(\mathbf{r})\right)}, \tag{8}$$

where

$$h\left(\eta_g\right) = \eta_g^3\left(6\eta_g^2 - 15\eta_g + 10\right) \tag{9}$$

is an interpolation parameter, such that $h(0) = 0$ and $h(1) = 1$. The local elasticity tensor at a given material point $\tilde{\boldsymbol{C}}(T, \mathbf{r})$ is defined as

$$\tilde{\boldsymbol{C}}(T, \mathbf{r}) = \frac{\sum_g \boldsymbol{C}^g(T) h\left(\eta_g(\mathbf{r})\right)}{\sum_g h\left(\eta_g(\mathbf{r})\right)}. \tag{10}$$

Note that within the diffuse grain boundaries, it is possible that $\sum_g h\left(\eta_g(\mathbf{r})\right) \neq 1$, that is why Eqs. (8) and (10) are normalized by $\sum_g h\left(\eta_g(\mathbf{r})\right)$. In this work, a linear interpolation of the values of elastic moduli (shown in Fig. 1b) between the temperature of 298 K and 673 K is used. Thus, the stress at a point $\mathbf{r}$ in the material is determined by

$$\tilde{\boldsymbol{\sigma}}(T, \mathbf{r}) = \tilde{\boldsymbol{C}}(T, \mathbf{r})(\boldsymbol{\epsilon}(\mathbf{r}) - \tilde{\boldsymbol{\epsilon}}_T(T, \mathbf{r})). \tag{11}$$

We approximated the constitutive behavior of α-U using small strain linear elasticity. We assumed mechanical equilibrium and the displacements throughout the material were determined by solving the stress divergence equation,

$$\nabla \cdot \tilde{\boldsymbol{\sigma}} = 0. \tag{12}$$

3.2. Phase Field Fracture

The phase field fracture model was adapted from the model of Miehe [31, 18] to incorporate anisotropic elastic constants by Zhang et al. [32]. Unlike classical fracture models, in which the crack is sharp, the phase field fracture model represents the crack surface as diffuse with a finite width. The crack phase field is non-smooth and is described by an exponential function; for a crack centered at $x = 0$,

$$c(x) = \exp\left(-\frac{|x|}{l}\right) \quad \text{for } -\infty < x < \infty, \tag{13}$$

where the diffuse crack profile is governed by the diffuse crack width l. For a full description of the phase field fracture model, see Ref. [32].

The crack field c evolves to minimize the total energy of the system, including the elastic energy due to deformation ($\dot{E}_E$) and the surface energy of the crack ($\dot{E}_D$). The rate of elastic energy release is defined as

$$\dot{E}_E = \frac{d}{dt}\int_\Omega \psi d\Omega, \tag{14}$$

where the elastic energy density of the material ψ is decomposed according to

$$\psi = g(c)\psi^+ + \psi^-. \tag{15}$$

ψ^+ and ψ^- are the portions of the strain energy density that contribute to crack propagation and that do not, respectively. $g(c)$ is an interpolation function that removes ψ^+ within a crack, defined as

$$g = (1 - c)^2(1 - b) + b, \tag{16}$$

where $b \ll 1$ is a numerical parameter which ensures positive definiteness of the system when $c = 1$. ψ^+ and ψ^- can be obtained from the stress and strain in various ways; here we employ the approach summarized in Ref. [32] that decomposes the energy density into its compressive (-) and tensile (+) parts and can consider anisotropic elastic constants. The non-cracked polycrystal stress $\tilde{\boldsymbol{\sigma}}$ is initially calculated using Eq. 11. This non-cracked stress is then decomposed using spectral decomposition

$$\tilde{\boldsymbol{\sigma}} = \boldsymbol{Q}\Lambda\boldsymbol{Q}^T, \tag{17}$$

where Λ is a diagonal matrix containing the principal stress tensor and $\boldsymbol{Q}$ is the eigenvector of the stress. The compressive and tensile parts of the stress are computed from the positive and negative projection tensors $\mathbf{P}$ (defined in Ref. [32]) according to,

$$\sigma^+ = \mathbf{P}^+\tilde{\boldsymbol{\sigma}} \tag{18}$$

$$\sigma^- = \mathbf{P}^-\tilde{\boldsymbol{\sigma}}, \tag{19}$$

and

$$\psi^+ = \frac{1}{2}\sigma^+ : \boldsymbol{\epsilon} \tag{20}$$

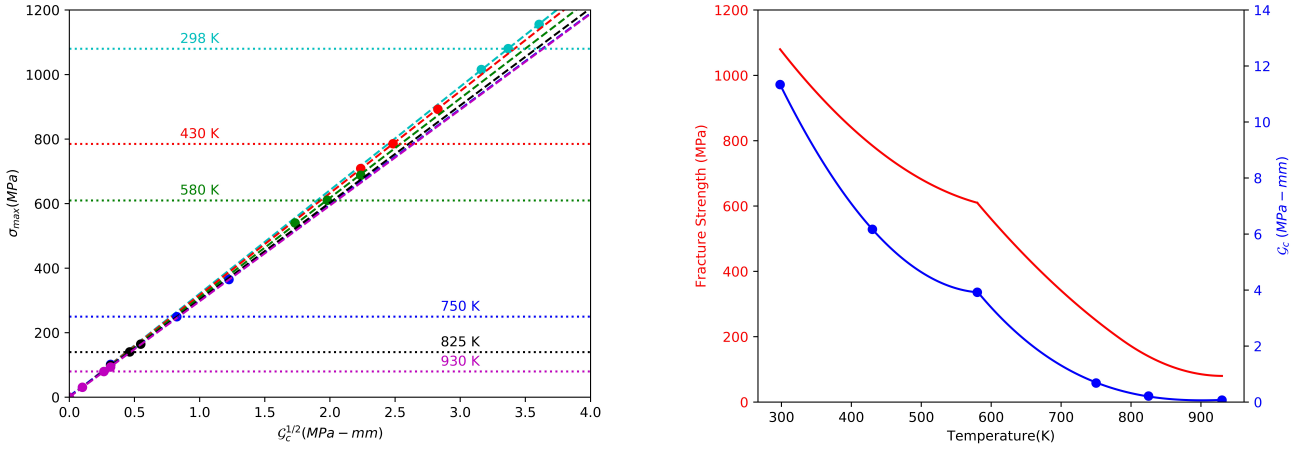

(a) (b)

Figure 2: Calibration of the $\mathcal{G}_c$ parameter using the experimental fracture strength reported by Rack and Knorovsky [33]. (a) Linear relationship of the maximum stress with the $\mathcal{G}_c$ parameter for different temperatures. The fracture stress at different temperatures is represented by the dotted line. Different colors represent the different temperatures considered. (b) Cubic interpolation (blue line) between the calibrated $\mathcal{G}_c$ values.

$$\psi^- = \frac{1}{2}\sigma^- : \epsilon. \tag{21}$$

The stress then be calculated from the strain energy as

$$\boldsymbol{\sigma} = \frac{\partial \psi}{\partial \boldsymbol{\epsilon}} = g(c)\frac{\partial \psi^+}{\partial \boldsymbol{\epsilon}} + \frac{\partial \psi^-}{\partial \boldsymbol{\epsilon}} \tag{22}$$

$$\boldsymbol{\sigma} = g(c)\boldsymbol{\sigma}^+ + \boldsymbol{\sigma}^-. \tag{23}$$

The surface energy of the crack can be described as

$$\dot{E}_D = \int_\Omega \mathcal{G}_c \dot{\gamma} d\Omega, \tag{24}$$

where $\mathcal{G}_c$ is the crack surface energy and $\dot{\gamma}$ is the crack surface density function per unit volume,

$$\dot{\gamma}(c, \nabla c) = \frac{1}{2l}c^2 + \frac{l}{2}|\nabla c|^2. \tag{25}$$

l is the crack width parameter.

The evolution of c is assumed to be quasistatic, such that there is no time derivative. The c and $\boldsymbol{\sigma}$ fields at a give strain increment are determined by solving the following equations:

$$\frac{dh}{dc}\left[\psi^+\right]_{max} + \frac{\mathcal{G}_c}{l}c - \nabla \cdot \left(\mathcal{G}_c l \nabla c\right) = 0, \tag{26}$$

$$\nabla \cdot \left(h\boldsymbol{\sigma}^+ + \boldsymbol{\sigma}^-\right) = 0. \tag{27}$$

$\left[\psi^+\right]_{max}$ is the maximum value of ψ^+ experienced at a given location throughout the simulation and it ensures that cracks do not heal.

The fracture model has two parameters, the diffuse crack width l and the crack surface energy $\mathcal{G}_c$. The crack width l is a model parameter, and its value is selected to minimize its impact on the predicted behavior. As the value of $l \to 0$, the crack behavior approaches that of a sharp crack. However, since the value for l must be greater than twice the element size to minimize discretization error [34], the computational cost increases as l decreases. In this work, we found the value $l = 1.2$ μm gave a good balance between accuracy and computational cost.

The surface energy $\mathcal{G}_c$ is a material property and its value was calibrated to represent the fracture stress of α-U reported by Rack and Knorovsky for various temperatures [33]. However, few details are given in that work about the experiments. It is safe to assume that the data were collected on polycrystalline samples and so they represent the average fracture stress of the material. Kuhn et al. [35] have shown that the fracture stress σ_{max} and $\mathcal{G}_c$ are related according to $\sigma_{max} = \beta\sqrt{\mathcal{G}_c}$, where β is a function of the crack width l and the elasticity tensor. An analytical form for β can be derived for some sample geometries, assuming isotropic elasticity. Due to the elastic anisotropy of α-U and the fact that we do not know the texture or crystal structure to relate to our single crystal elastic constants, an analytical form for β is not possible. Therefore, we estimated the values of $\mathcal{G}_c$ at various temperatures for $l = 1.2$ μm by carrying out simulations of single crystal single edge notch tension (SENT) specimens, assuming that the crystal structure was aligned with the lab reference frame. We determined the values of $\mathcal{G}_c$ at temperatures ranging from 298 K to 930 K that resulted in the reported fracture stress. Figure 2a plots σ_{max} versus $\sqrt{\mathcal{G}_c}$ for increasing temperatures. The slope changes with temperature due to the impact of temperature on the elasticity tensor (see Fig. 1b). The relationship between $\mathcal{G}_c$ and temperature was determined for α-U by fitting a cubic spline to the results. Figure 2b shows the fracture stress from Rack and Knorovksy [33] and the calibrated values of $\mathcal{G}_c$ for the temperatures of interest in this work. Though this approach

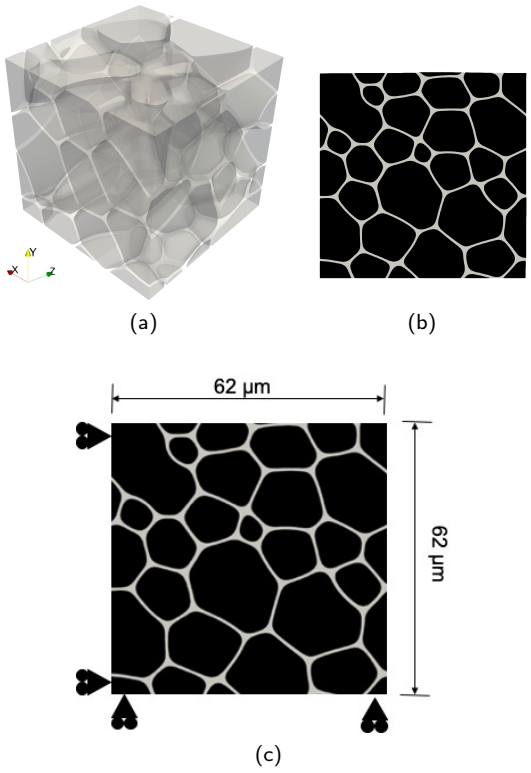

Figure 3: The grain structure and boundary conditions used in the simulations, with an average grain size of 20 μm; (a) Three-dimensional simulation domain; (b) Two-dimensional simulation domain; (c) Mechanical boundary conditions used in the simulations, presented here for the two-dimensional domain.

only approximates the fracture behavior of α-U, it is sufficient for us to investigate the impact of anisotropic thermal expansion on fracture.

α-U experiences intergranular fracture in the temperature range considered in this work. Thus, we assumed intergranular fracture is the preferred fracture mode and grain boundaries are the preferred location for fracture. To encourage intergranular fracture, we made $\mathcal{G}_c$ heterogeneous, with the calibrated $\mathcal{G}_c$ values applied at grain boundaries (regions where $1 < \eta^{\mathcal{G}} < 0$) and $4 \times \mathcal{G}_c$ applied within the grains. Since we interpolate the thermal strain and the elasticity tensor across the grain boundaries, as shown in Eqs. (8) and (10), this means that cracks primarily form within regions of the material where we have approximated the mechanical response. However, since the elastic energy that drives crack formation is a long-range field impacted by the surrounding material, any error introduced by it will not impact the general trends regarding the impact of thermal expansion anisotropy on fracture.

3.3. Initial and Boundary Conditions

The initial grain structures were generated by running a 2D and a 3D phase-field grain growth simulation [36]; the resulting grain structures were used in the thermal expansion simulations. The grain structures were initialized via a Voronoi tessellation and then allowed to evolve to develop a more realistic structure (Figs. 3a and 3b). The final average grain size was 20 μm and the grains were equiaxed. The 3D computational domain was $(62\ \mu\text{m})^3$ with 30 grains and the 2D domain was $(62\ \mu\text{m})^2$ with 30 grains; each grain was assigned a random orientation which remained constant throughout the simulation.

The mechanical boundary conditions were designed to allow the domain to deform freely without any rigid body motion. On each coordinate axis, the plane that passed through the origin with normal parallel to that axis had an applied Dirichlet boundary condition with zero displacements in the corresponding direction, as represented in Fig. 3c. All other displacements were unconstrained.

3.4. Numerical Methods

The phase-field fracture model was implemented using the open-source Multiphysics Object-Oriented Simulation Environment (MOOSE) [37] in a similar manner to that described in Ref. [34]. The 3D domains were meshed with eight-node hexahedral elements and the 2D domains with four-node quadrilateral elements. For all non-linear variables, linear Lagrange shape functions were used. The system of nonlinear equations was solved using Newton's method. The matrix preconditioning was carried in all simulations using the Additive Schwarz Method with incomplete LU factorization for sub-preconditioning. For the time integration scheme, a second-order backward Euler differentiation scheme was applied with a time step size of $10^{-6}s$.

For the grain growth simulation, adaptive meshing, adaptive time stepping, and the GrainTracker algorithm [36] were used to reduce the computational cost. Each grain for the grain growth simulation is generally represented by one order parameter to avoid nonphysical merging of grains during grain growth and to assign unique properties. The GrainTracker algorithm reduces the number of phase-field order parameters needed to avoid grain merging and assigns each grain a unique ID separate from its order parameter value. Fourteen order parameters (nonlinear variables) were needed for the 3D grain growth simulations. The minimum element size was 0.6 μm, while the maximum element size was 2.38 μm and gradient jump indicators [38] were used to determine mesh adaptivity.

4. Results and Discussions

A series of simulations were run to investigate intergranular fracture in polycrystals due to thermal stresses caused by anisotropic thermal expansion and contraction. In the simulations, temperatures ranged from room temperature to around 673 K. In Section 4.1, we compare the fracture in 3D polycrystals with a random crystallographic texture during heating and cooling. In Section 4.2, we investigate the impact of crystallographic texture on the fracture and net shape change of 3D polycrystals. Section 4.3 uses 2D simulations of specific planes to determine which crystallographic directions are the primary cause of the observed fracture behavior. Note that two different coordinate systems are used in this

work, each described by a different notation. The crystallographic coordinate system is described with Miller indices for planes and directions. The laboratory coordinate system for the polycrystalline aggregate is described using x, y, and z notation.

4.1. Comparison between heating and cooling

In polycrystalline materials with anisotropic thermal expansion, any change in temperature, whether an increase or decrease, will result in stress between grains and could result in fracture. In this section, we use our phase-field fracture model to compare the fracture during heating and cooling using identical 3D α-U polycrystals with a random crystallographic texture. In the heating case, we heat the polycrystal from an initial temperature of 298 K to 673 K (with the stress-free temperature $T_0 = 298$ K). In the cooling case, we cool the polycrystal from an initial temperature of 673 K to 300 K (with $T_0 = 673$ K). The heating case is representative of a material that has reached its equilibrium state at room temperature and then is heated; the cooling case is representative of a material that has been manufactured at high temperature and then is cooled to room temperature. We repeated the simulations using different sets of random orientations assigned to each grain, and the results did not vary significantly. The results shown in this section use one of these sets of orientations and are representative of the average behavior.

Figures 4a and 4b show the maximum principal stress (MPS) σ throughout the domain due to the anisotropic thermal expansion during heating. The 3D domains are visualized at two different temperatures, one at an average temperature of 570 K, when cracks first nucleated (Fig. 4a), and the other at an average temperature of 673 K, at the end of the simulation (Fig. 4b). The black regions represent cracks. Our results show that the largest MPS occurs near grain boundaries, consistent with what has been observed in previous work [7, 8, 9]. The large MPS at the grain boundaries, along with the smaller $\mathcal{G}_c$, resulted in intergranular fracture.

During cooling, stresses again developed between the grains and eventually caused fracture. Figures 4c and 4d show the MPS at the time of fracture nucleation (average temperature of 557 K) and near the end of the simulation (average temperature of 300 K), respectively. The cooling case resulted in larger values of MPS than in the heating case and more of the polycrystal experienced a large MPS, since more of the polycrystal is in tension during cooling than during heating. As seen in the heating case, the largest MPS was found at grain boundaries and resulted in fracture. A larger fraction of the grain boundaries fractured in the cooling case than in the heating case.

To quantitatively compare the fracture of the two cases, it is useful to quantify the total crack surface area. This value is calculated in the phase-field fracture simulation by first calculating the total volume in the simulation domain for which $c > 0.9$ using a flood algorithm; this represents the total diffuse crack volume. We approximated this volume as a rectangle and divided by the crack thickness $2l$ to obtain the area of one side of the crack.

The total crack area and the maximum values of the volumetric stress components for the heating case are shown as a function of the change in temperature ($T - T_0$ for heating and $T_0 - T$ for cooling for ease of comparison) in Fig. 4e. The maximum values of the three stress components have very similar values until a change of about 125 K, at which point they diverged and σ_{yy} reached the largest maximum value. Fracture began just after a change of 250 K, and crack propagation accelerated at a change of around 275 K. As the cracks propagated, all components of the stress decreased. The predicted behavior agrees well with results from Ref. [23] showing that a temperature interval greater than 200 K resulted in void creation in α-U.

Figure 4e also shows the total fracture area and the maximum tensile stress for each component for the cooling case. The stress increased rapidly at the start of the simulation and fracture initiated after a change of only 100 K. The high stresses in the simulation are due, in part, to the fact that the anisotropy of the CTE of α-U is higher at elevated temperature [1]. The stress peaked and started to decrease once fracture initiated at a change of approximately 125 K. As the temperature dropped, the fracture strength also dropped and subsequently slowed down the crack propagation. This resulted in an eventual increase in stress.

The stress increased much more rapidly with temperature change in the cooling case than in the heating case, and the maximum values of the different stress components varied significantly throughout the change in temperature in the cooling case, while the different components all had similar maximum values for the first two-thirds of the change in the heating case. This is because there is large anisotropy in the CTE at the beginning of the cooling simulation (at high temperature), while there is lower anisotropy at the beginning of the heating simulation (at low temperature). Due to the high stress, fracture initiated much earlier in the cooling simulation (at $\Delta T \approx 100$ K) than in the heating simulation (at $\Delta T \approx 250$ K), and the total crack area at the end of the simulations was more than one and half times larger in the cooling simulation. These results clearly indicate that fracture is more likely to occur upon cooling than heating in α-U for materials that were first equilibrated before changing the temperature. This would be the case for any material for which the anisotropy increases with temperature.

4.2. Effect of crystallographic texture

In section 4.1, we modeled fracture in a material with a random crystallographic texture. The stress built up between grains because the CTE anisotropy caused each grain to change shape in a different manner; thus, the misorientation between grains must have some impact on the stress and thus the fracture. In this section, we investigate the effect of crystallographic texture using simulations with four additional sets of crystal orientations for the polycrystal; the random orientations from the previous section will be included in the investigation. The other cases include a duplex case, and three cases of similar orientations with misorien-

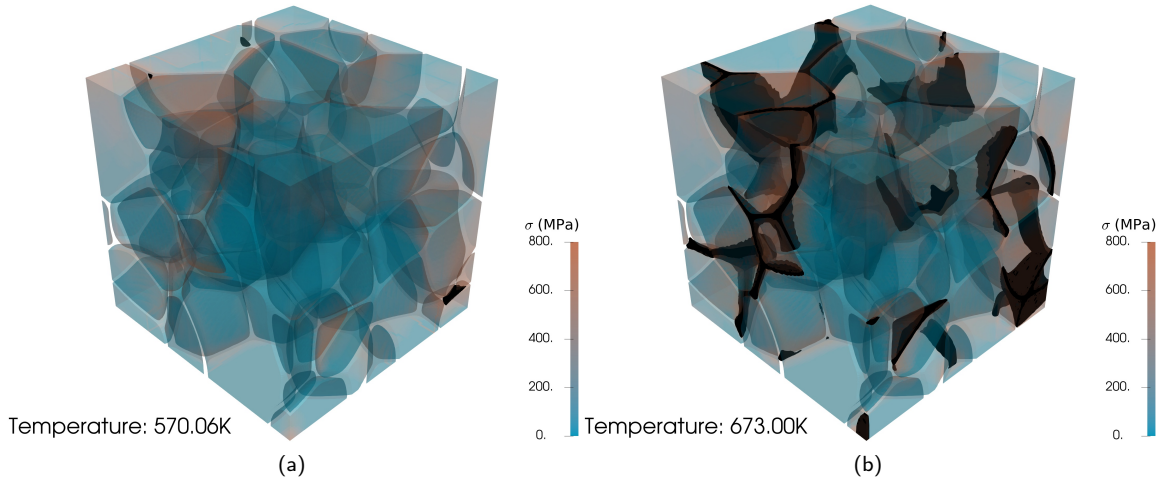

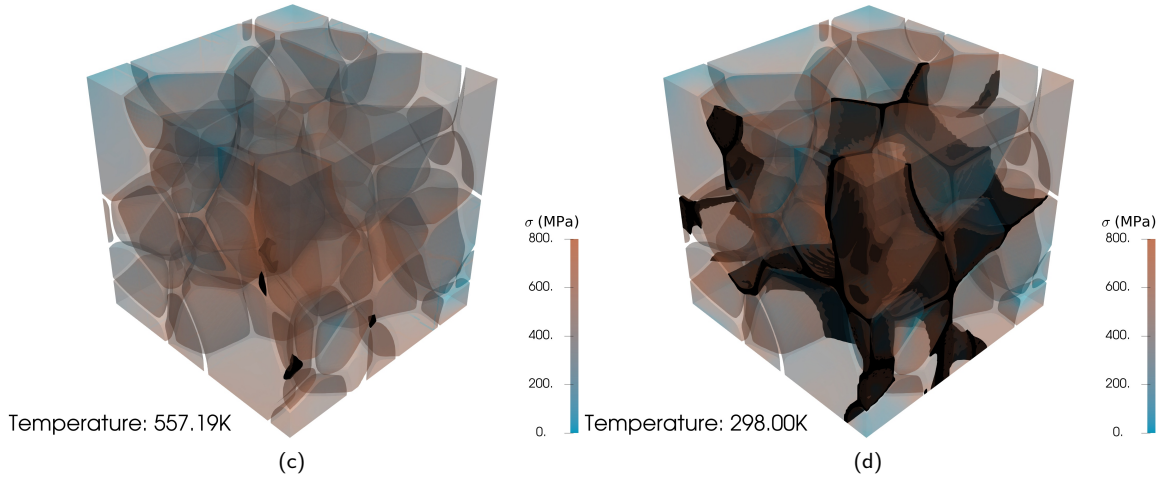

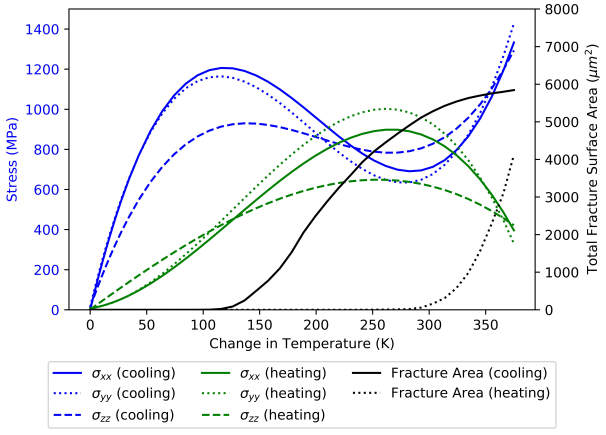

(e)

Figure 4: Fracture simulation results during heating and cooling, where (a) and (b) show the polycrystals at crack initiation and at the simulation end, respectively, during heating. (c) and (d) show the same during cooling. The cracked regions are shown in black and the domain is shaded by MPS σ. (e) shows the progression of fracture with change in temperature for both heating and cooling, including the total fracture surface area and the maximum values of the three volumetric stresses.

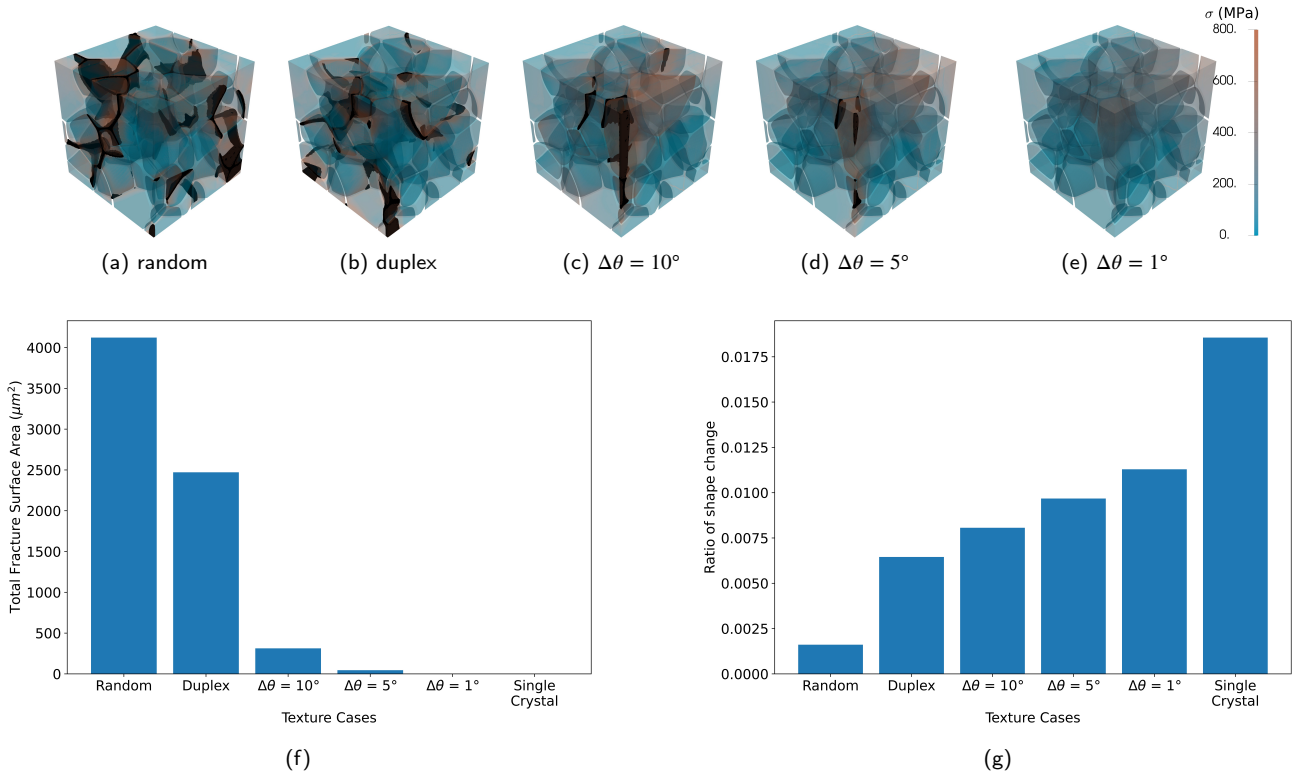

Figure 5: The impact of crystallographic texture on fracture, where (a)-(e) show the final polycrystals for the various texture cases. The cracks are shown in black and the images are shaded by MPS σ. (f) shows the total crack surface area for the various texture cases, indicating that the total crack area increases with misorientation. (g) shows the ratio of shape change for the various cases, indicating that the shape change tends to decrease with misorientation. Single crystal crack length and shape change are provided for comparison.

tations $\leq 10°$, $\leq 5°$, and $\leq 1°$. In the duplex case, the orientations are distributed into two distinct sets of orientations with mean Eular angle of [33° 68° 262°] and [123° 158° 353°] respectively. There is a misorientation of $\leq 5°$ within the sets. For all the texture cases, we simulated heating from room temperature to 673 K, as was done in the previous section.

The final microstructure at the end of the heating for each of the five cases are shown in Figs. 5a-5e. From the microstructures, it is clear that the amount of fracture is much larger for the random and duplex textures than for the other cases. However, it is difficult to make a quantitative comparison by comparing the microstructures. Therefore, we have plotted the total fracture surface area (Fig. 5f) at the end of each simulation from the various texture cases. In a single crystal, anisotropic thermal expansion results in a net shape change rather than fracture, since there is no heterogeneity in the strain. Therefore, we also quantify the net shape change of the polycrystals with a ratio of shape change, R, as defined by

$$R = \frac{d_{\max} - d_{\min}}{d_0}, \tag{28}$$

where d_0 is the initial side length of the computational domain, $d_{\min}$ is the minimum side length of the computational domain at the final temperature, and $d_{\max}$ is the maximum side length, as shown in Fig. 5g. For comparison, values from a single crystal are also shown.

The total crack surface area at the end of the simulations decreased as the misorientation decreased, with the random case having the largest crack surface area and the case with misorientations $\leq 1°$ having no cracks. The ratio of the shape change showed the opposite trend; the shape change increased as the misorientation decreased. When the grains are highly misoriented, they cause high internal stresses that result in fracture, but the anisotropy is averaged out and little shape change occurs. When the grains are only slightly misoriented, the internal stresses are small and do not cause significant fracture, but they also do not average out the anisotropy so that there is significant shape change.

4.3. How the anisotropy in thermal expansion contributes to the stress development in the polycrystal

The previous sections have established that CTE anisotropy results in sufficient stress to induce intergranular fracture in polycrystals with significant misorientation between grains. To further investigate the cause of the stress development and subsequent fracture, we performed 2D simulations using only 2 of the crystallographic planes.

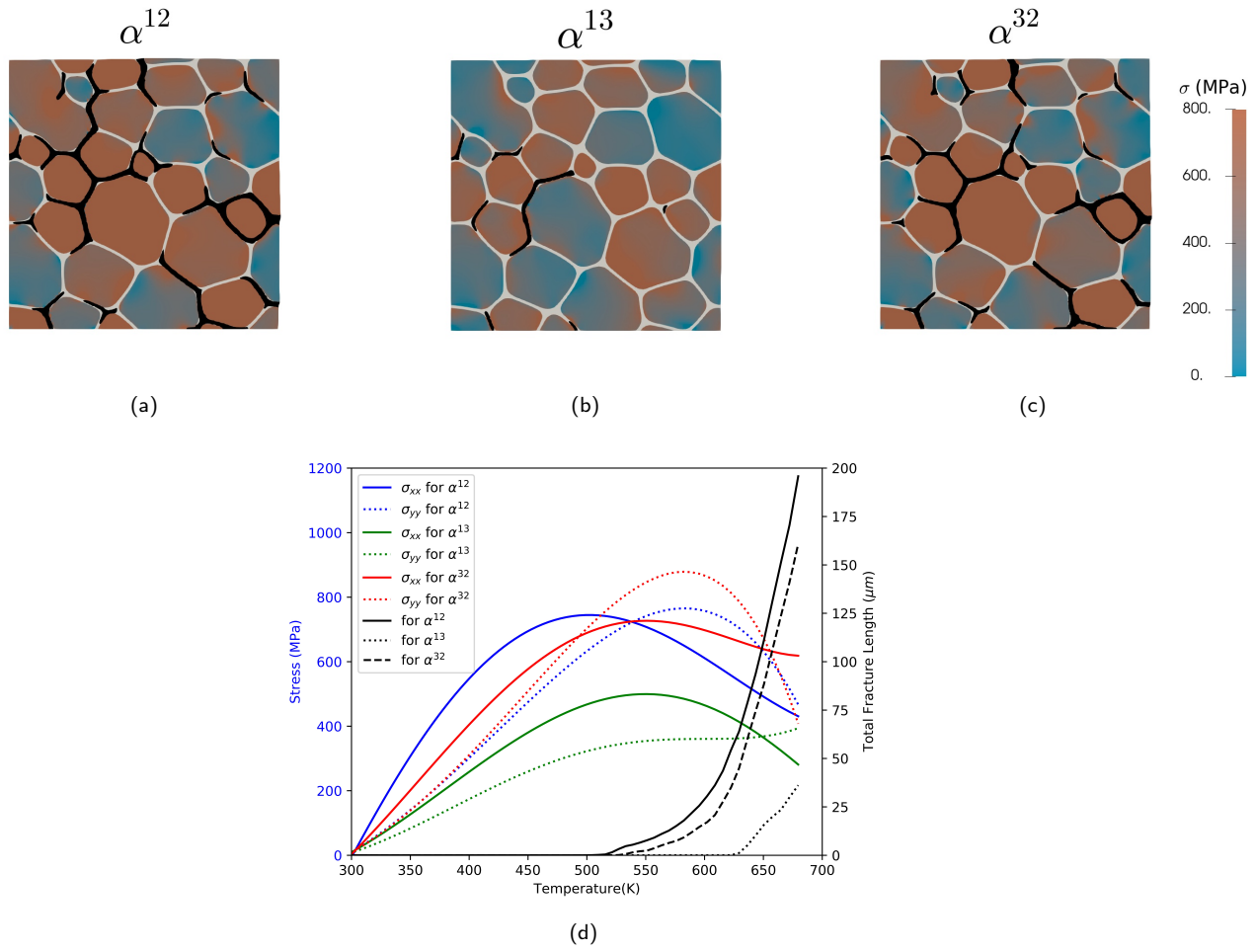

Figure 6: 2D fracture simulation results, where (a) - (c) shows the final 2D polycrystals for the α^{12}, α^{13}, and α^{32} cases, respectively. The cracks are shown in black area and polycrystals are shaded by the MPS σ. (d) shows the progression of the total fracture length and the maximum value for the two volumetric stresses with temperature. The black lines represents the fracture length. Significant fracture only occurred in the two cases that included the thermal expansion in the [010] direction.

In the 3D case, the CTE tensor α was defined by Eq. (2). For this study, we employed three 2D cases with the α tensors defined as

$$\alpha^{12} = \begin{bmatrix} \alpha_{[100]} & 0 \\ 0 & \alpha_{[010]} \end{bmatrix}$$
$$\alpha^{13} = \begin{bmatrix} \alpha_{[100]} & 0 \\ 0 & \alpha_{[001]} \end{bmatrix}$$
$$\alpha^{32} = \begin{bmatrix} \alpha_{[001]} & 0 \\ 0 & \alpha_{[010]} \end{bmatrix}.$$

The 2D simulations were performed assuming linear elasticity and one Euler angle was used to describe the orientation of the grains about the out of plane axis.

Figures 6a - 6c show the cracks in the 2D domains at the end of the simulations for the α^{12}, α^{13}, and α^{32} cases, respectively. Each is shaded by the MPS and the cracks are shown in black. The stresses and cracks in the α^{12} and the α^{32} cases were similar. The stresses in the α^{13} case were much lower and very few cracks formed, compared to the other two cases.

Figure 6d shows the maximum principal stress and the total fracture length with temperature from the three 2D cases. The stresses in the α^{12} and α^{32} cases increased at similar rates, but the stresses increased much slower in the α^{13} case. Fracture initiated at the lowest temperature in the α^{12} case and at a slightly higher temperature in the α^{32} case, such that the final fracture length was larger in the α^{12} case. As stated previously, fracture occurred late in the α^{13} case and the cracks propagated slowly. Thus, the case that does not include the thermal expansion in the [010] direction did not experience sufficient stress to fracture, indicating that the unique CTE behavior of the [010] direction is what drives the fracture for the case of α-U. More generally, the largest difference between the CTE behavior in the three crystallographic directions dominates the fracture behavior.

5. Conclusion

Polycrystalline materials with anisotropic thermal expansion can experience fracture due to changes in temper-

ature. In this study, we have investigated the impact of anisotropic thermal expansion with phase-field fracture simulations using α-U as a model material. The model assumed brittle fracture and a heterogeneous energy release rate, with lower values on grain boundaries encouraging intergranular fracture.

The 3D fracture simulations showed significant thermal stress induced along grain boundaries, resulting in intergranular fracture. Fracture initiated much earlier and the final cracks were much more extensive during cooling than during heating since the anisotropy in α-U is more pronounced at high temperature. The total fracture area increased with grain misorientation, while the net shape change decreased. This is because highly misorientated grains deform in different directions, causing internal stress but averaging out the anisotropy. Two-dimensional simulations that only involved two of the three crystallographic planes showed that the largest difference between the CTE in the three crystallographic directions dominates the fracture.

Mesoscale simulations allow the study of the impact of anisotropic thermal expansion and crystallographic texture in a way that is difficult or impossible to achieve via experiments. These studies provide both basic scientific insight and engineering support by predicting and explaining the complex behavior of anisotropic materials. They can offer a path forward for designing and fabricating novel materials; in addition, engineering decisions regarding workpiece design and behavior in service can be made more efficiently and with fewer prototype iterations.

Acknowledgment

This research made use of the resources of the High Performance Computing Center at Idaho National Laboratory, which is supported by the Office of Nuclear Energy of the U.S. Department of Energy and the Nuclear Science User Facilities under Contract No. DE-AC07-05ID14517. This work was funded by the Department of Energy Nuclear Energy Advanced Modeling and Simulation program. This manuscript has been authored by Battelle Energy Alliance, LLC under the aforementioned contract Contract No. DE-AC07-05ID14517. The United States Government retains and the publisher, by accepting the article for publication, acknowledges that the United States Government retains a nonexclusive, paid-up, irrevocable, world-wide license to publish or reproduce the published form of this manuscript, or allow others to do so, for United States Government purposes.

Data Availability Statement

The raw and processed data required to reproduce these findings cannot be shared at this time due to technical reasons. All data and input files used in this work will be provided upon request.

References

[1] Lowell T Lloyd and CS Barrett. Thermal expansion of alpha uranium. *Journal of Nuclear Materials*, 18(1):55–59, 1966.

[2] Gang Liu, Zhibin Gao, and Jie Ren. Anisotropic thermal expansion and thermodynamic properties of monolayer β-te. *Physical Review B*, 99(19):195436, 2019.

[3] Henry Y. B. Mar and William D. Scott. Fracture Induced in Al2O3 Bicrystals by Anisotropic Thermal Expansion. *Journal of the American Ceramic Society*, 53(10):555–558, 1970.

[4] J. A. Kuszyk and R. C. Bradt. Influence of Grain Size on Effects of Thermal Expansion Anisotropy in MgTi2O5. *Journal of the American Ceramic Society*, 56(8):420–423, 1973.

[5] Yutaka Ohya, Zenbe-e Nakagawa, and Kenya Hamano. Grain-Boundary Microcracking Due to Thermal Expansion Anisotropy in Aluminum Titanate Ceramics. *Journal of the American Ceramic Society*, 70(8):C–184–C–186, 1987.

[6] M. H Zimmerman, D. M Baskin, K. T Faber, E. R Fuller, A. J Allen, and D. T Keane. Fracture of a textured anisotropic ceramic. *Acta Materialia*, 49(16):3231–3242, September 2001.

[7] A. G. Evans. Microfracture from thermal expansion anisotropy–I. Single phase systems. *Acta Metallurgica*, 26(12):1845–1853, December 1978.

[8] Viggo Tvergaard and John W. Hutchinson. Microcracking in Ceramics Induced by Thermal Expansion or Elastic Anisotropy. *Journal of the American Ceramic Society*, 71(3):157–166, 1988.

[9] Narayanaswamy Sridhar, Wuhua Yang, David J. Srolovitz, and Edwin R. Fuller. Microstructural Mechanics Model of Anisotropic-Thermal-Expansion-Induced Microcracking. *Journal of the American Ceramic Society*, 77(5):1123–1138, 1994.

[10] M. Ortiz and S. Suresh. Statistical Properties of Residual Stresses and Intergranular Fracture in Ceramic Materials. *Journal of Applied Mechanics*, 60(1):77–84, March 1993.

[11] GA Malygin and VA Likhachev. Anisotropy of thermal expansion and thermal microstresses. *Zavodskaya Lab*, (3):335–347, 1966.

[12] WJM Tegart. Tensile properties of polycrystalline cadmium and some cadmium alloys in range-196 to 200 degrees c. *JOURNAL OF THE INSTITUTE OF METALS*, 91(3):99, 1962.

[13] FJP Clarke. Residual strain and the fracture stress-grain size relationship in brittle solids. *Acta Metallurgica*, 12(2):139–143, 1964.

[14] RW Armstrong and NR Borch. Thermal microstresses in beryllium and other hcp materials. *Metallurgical and Materials Transactions B*, 2(11):3073–3077, 1971.

[15] Long-Qing Chen. Phase-field models for microstructure evolution. *Annual review of materials research*, 32(1):113–140, 2002.

[16] Nele Moelans, Bart Blanpain, and Patrick Wollants. An introduction to phase-field modeling of microstructure evolution. *Calphad*, 32(2):268–294, 2008.

[17] Michael R Tonks and Larry K Aagesen. The phase field method: mesoscale simulation aiding material discovery. *Annual Review of Materials Research*, 49:79–102, 2019.

[18] Christian Miehe, Martina Hofacker, and Fabian Welschinger. A phase field model for rate-independent crack propagation: Robust algorithmic implementation based on operator splits. *Computer Methods in Applied Mechanics and Engineering*, 199(45-48):2765–2778, 2010.

[19] Marreddy Ambati, Tymofiy Gerasimov, and Laura De Lorenzis. A review on phase-field models of brittle fracture and a new fast hybrid formulation. *Computational Mechanics*, 55(2):383–405, 2015.

[20] CS Barrett, MH Mueller, and RL Hitterman. Crystal structure variations in alpha uranium at low temperatures. *Physical Review*, 129(2):625, 1963.

[21] Benjamin Beeler, Chaitanya Deo, Michael Baskes, and Maria Okuniewski. First principles calculations of the structure and elastic constants of α, β and γ uranium. *Journal of Nuclear Materials*, 433(1-3):143–151, 2013.

[22] Michael J Mehl, David Hicks, Cormac Toher, Ohad Levy, Robert M Hanson, Gus Hart, and Stefano Curtarolo. The aflow library of crystallographic prototypes: part 1. *Computational Materials Science*, 136:S1–S828, 2017.

[23] CL Angerman and GR Caskey Jr. Swelling of uranium by mechanical cavitation. *Journal of Nuclear Materials*, 13(2):182–196, 1964.

[24] HH Chiswik, AE Dwight, LT Lloyd, MV Nevitt, and ST Zegler. Advances in the physical metallurgy of uranium and its alloys. Technical report, Argonne National Lab., Lemont, Ill., 1958.

[25] RC Lobb. Void nucleation during thermal cycling of adjusted uranium. *Journal of Nuclear Materials*, 48(1):67–73, 1973.

[26] ES Fisher. Temperature dependence of the elastic moduli in alpha uranium single crystals, part iv (298 to 923 k). *Journal of Nuclear Materials*, 18(1):39–54, 1966.

[27] DMR Taplin. *Mechanical behaviour & fracture of uranium*. PhD thesis, University of Oxford, 1964.

[28] MF Nolan. Mechanical properties of dilute uranium alloys at elevated temperatures. Technical report, Mallinckrodt Chemical Works, Weldon Spring, Mo. Uranium Div., 1966.

[29] VK Golubev. Strength and fracture of uranium, plutonium and several their alloys under shock wave loading. In *EPJ Web of Conferences*, volume 26, page 02015. EDP Sciences, 2012.

[30] Danan Fan and L-Q Chen. Computer simulation of grain growth using a continuum field model. *Acta Materialia*, 45(2):611–622, 1997.

[31] Christian Miehe, Fabian Welschinger, and Martina Hofacker. Thermodynamically consistent phase-field models of fracture: Variational principles and multi-field fe implementations. *International Journal for Numerical Methods in Engineering*, 83(10):1273–1311, 2010.

[32] Shuaifang Zhang, Wen Jiang, and Michael R Tonks. A new phase field fracture model for brittle materials that accounts for elastic anisotropy. *Computer Methods in Applied Mechanics and Engineering*, page In Press, 2019.

[33] Henry J Rack and Gerald A Knorovsky. Assessment of stress-strain data suitable for finite-element elastic–plastic analysis of shipping containers. Technical report, Sandia Labs., 1978.

[34] Pritam Chakraborty, Yongfeng Zhang, and Michael R Tonks. Multiscale modeling of microstructure dependent intergranular brittle fracture using a quantitative phase-field based method. *Computational Materials Science*, 113:38–52, 2016.

[35] Charlotte Kuhn, Alexander Schlüter, and Ralf Müller. On degradation functions in phase field fracture models. *Computational Materials Science*, 108:374–384, 2015.

[36] Cody J Permann, Michael R Tonks, Bradley Fromm, and Derek R Gaston. Order parameter re-mapping algorithm for 3d phase field model of grain growth using fem. *Computational Materials Science*, 115:18–25, 2016.

[37] Derek R Gaston, Cody J Permann, John W Peterson, Andrew E Slaughter, David Andrš, Yaqi Wang, Michael P Short, Danielle M Perez, Michael R Tonks, Javier Ortensi, et al. Physics-based multiscale coupling for full core nuclear reactor simulation. *Annals of Nuclear Energy*, 84:45–54, 2015.

[38] Benjamin S Kirk, John W Peterson, Roy H Stogner, and Graham F Carey. libmesh: a c++ library for parallel adaptive mesh refinement/coarsening simulations. *Engineering with Computers*, 22(3-4):237–254, 2006.